Impact of Spin-Entropy on the Thermoelectric Properties of a 2D Magnet

Canetta, Alessandra; Volosheniuk, Serhii; Satheesh, Sayooj; Alvarinhas Batista, José Pedro; Castellano, Aloïs; Conte, Riccardo; Chica, Daniel George; van der Zant, Herre S.J.; Gehring, Pascal; More Authors

DOI
10.1021/acs.nanolett.4c00809

Publication date
2024

Document Version
Final published version

Published in
Nano Letters

NANO LETTERS

pubs.acs.org/NanoLett Letter

Impact of Spin-Entropy on the Thermoelectric Properties of a 2D Magnet

Alessandra Canetta, Serhii Volosheniuk, Sayooj Satheesh, José Pedro Alvarinhas Batista, Aloïs Castellano, Riccardo Conte, Daniel George Chica, Kenji Watanabe, Takashi Taniguchi, Xavier Roy, Herre S. J. van der Zant, Marko Burghard, Matthieu Jean Verstraete, and Pascal Gehring*

Cite This: *Nano Lett.* 2024, 24, 6513−6520 Read Online

ACCESS | Metrics & More | Article Recommendations | Supporting Information

ABSTRACT: Heat-to-charge conversion efficiency of thermoelectric materials is closely linked to the entropy per charge carrier. Thus, magnetic materials are promising building blocks for highly efficient energy harvesters as their carrier entropy is boosted by a spin degree of freedom. In this work, we investigate how this spin-entropy impacts heat-to-charge conversion in the A-type antiferromagnet CrSBr. We perform simultaneous measurements of electrical conductance and thermocurrent while changing magnetic order using the temperature and magnetic field as tuning parameters. We find a strong enhancement of the thermoelectric power factor at around the Néel temperature. We further reveal that the power factor at low temperatures can be increased by up to 600% upon applying a magnetic field. Our results demonstrate that the thermoelectric properties of 2D magnets can be optimized by exploiting the sizable impact of spin-entropy and confirm thermoelectric measurements as a sensitive tool to investigate subtle magnetic phase transitions in low-dimensional magnets.

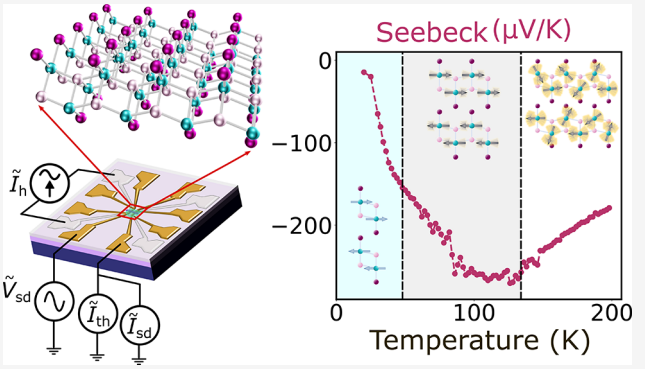

KEYWORDS: *2D magnetism, CrSBr, thermoelectric, entropy*

The Seebeck coefficient (α) quantifies the electromotive force or gradient of the electrochemical potential $\nabla V = \nabla\tilde{\mu}/q$ developing in a material exposed to a temperature gradient ∇T (Figure 1), and is the central parameter that determines the efficiency of a thermoelectric device.[1,2] As the electrochemical potential $\tilde{\mu}$ of a population of electrically charged particles consists of the sum of the chemical potential μ and the electrostatic contribution $q\varphi$, the Seebeck coefficient can be written as[3]

$$\alpha = -\frac{\partial\tilde{\mu}}{q\partial T} = -\frac{\partial\mu}{q\partial T} - \frac{\partial\varphi}{\partial T} \tag{1}$$

where q is the elementary charge. The second term of eq 1, often referred to as the effective Seebeck coefficient, contains dynamical effects linked to scattering/carrier relaxation processes.[3,4] In contrast, the first component—known as the Kelvin formula[5,6]—is purely thermodynamic. On the basis of thermodynamic considerations for an electronic system, this term is directly related to the average entropy transported per charge carrier[1,7] using the Maxwell equation $\left(\frac{\partial\mu}{\partial T}\right)_N = -\left(\frac{\partial S}{\partial N}\right)_T$, where N is the mean time-averaged population of the system and S is the electronic entropy.[7−9] This implies that all mechanisms that increase the entropy per carrier can enhance the Seebeck coefficient. In particular, the spin degrees of freedom of carriers in magnetic materials can lead to such increased entropy,[7,10−12] as these correspond to more phase space for the same number of electrons (especially the magnetically active d electrons). The different types of entropy will affect the electronic states (band energies and electron density) and the chemical potential, which then modifies the Seebeck coefficient, as shown in eq 1. Figure 1 illustrates this concept by comparing the Seebeck effect of an antiferromagnet in three temperature regimes linked to different magnetic phases. In all cases, under open-circuit conditions, a thermally driven diffusion current of charge carriers (red arrows) from the heated region (depicted in orange) to the cold one (in blue) is balanced by a drift current generated by an electric field that builds up inside the material. Additionally, the so-called *spin-entropy*, S_m, in magnetic materials can contribute to

Received: February 15, 2024
Revised: April 16, 2024
Accepted: April 17, 2024
Published: April 23, 2024

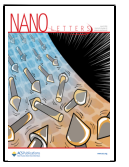

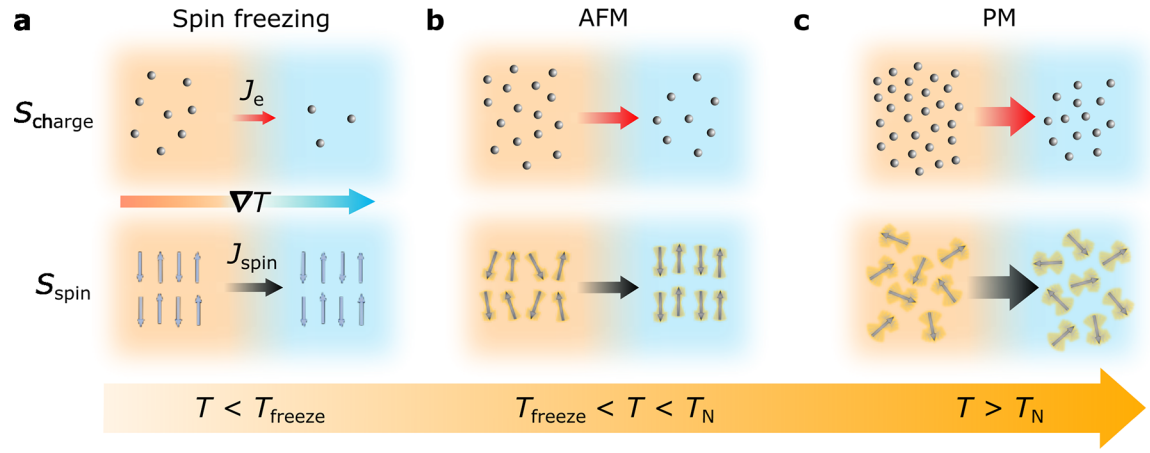

Figure 1. Seebeck effect in nonmagnetic and magnetic materials. Schematic illustrating the working principle of the Seebeck effect in a material in different magnetic phases. The three images refer to different temperature ranges and consequently magnetic phases: "spin freezing" state (a), antiferromagnetic (AFM) state (b), and paramagnetic (PM) state (c). The top pictures show the thermally driven diffusion of the charge carriers, of which direction and magnitude are qualitatively indicated by the red arrows. The bottom images show the additional contribution of the spin-entropy (S_m) to the Seebeck coefficient. Direction and magnitude of the entropy flow are qualitatively indicated by the black arrows.[1,7] Temperature ranges are indicated in the large orange arrow at the bottom of the figure, while, in a), the direction of the temperature gradient is illustrated by an orange-to-blue arrow.

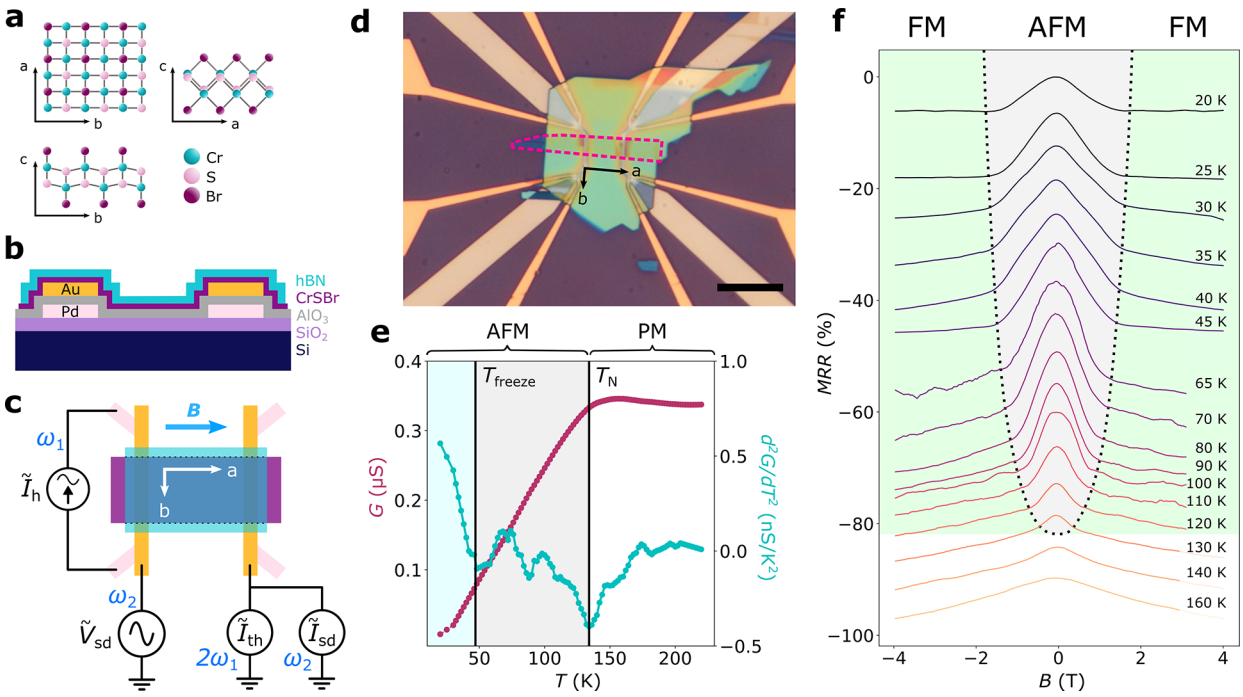

Figure 2. Crystal structure, measurement setup, and electrical transport of CrSBr. (a) Crystal structure of CrSBr, from the *c* axis (top left), *b* axis (top right) and *a* axis (bottom). Cr, S and Br atoms are represented as cyan, pink and purple spheres, respectively. (b) Side view of the device. (c) Schematic of the setup used for magneto-transport and thermoelectric measurements. (d) Optical image of the measured device. The magenta dashed guideline highlights the position of the CrSBr flake, covered by the hBN layer. (e) Temperature dependence of the conductance *G* (purple) and the second derivative of the conductance $\frac{d^2G}{dT^2}$ (cyan). The white region and the light blue/gray region correspond respectively to the paramagnetic (PM) and antiferromagnetic (AFM) phases of CrSBr. (f) Magneto-resistance ratio (MRR) versus the applied magnetic field *B* at different temperatures between 20 and 160 K. An offset of 6% is applied for clarity between each pairs of curves. The AFM and FM magnetic phases are shaded in gray and green, respectively. The black dotted line defines the saturation field H_S (see Supporting Information section S9). Scale bar in (d): 10 μm.

their Seebeck effect (bottom panels of Figure 1).[1,7] S_m is minimum below the "spin freezing" temperature (Figure 1a, a special magnetic state in CrSBr, see discussion below). Thermal fluctuations will then increase S_m (Figure 1b), which reaches its maximum above the phase transition temperature, as the material enters the paramagnetic (PM) state (Figure 1c).[1]

In this context, thanks to their controllable magnetism,[13−16] two-dimensional (2D) magnets provide an ideal platform to test this effect. Among the layered van der Waals (vdW)

https://doi.org/10.1021/acs.nanolett.4c00809
Nano Lett. 2024, 24, 6513−6520

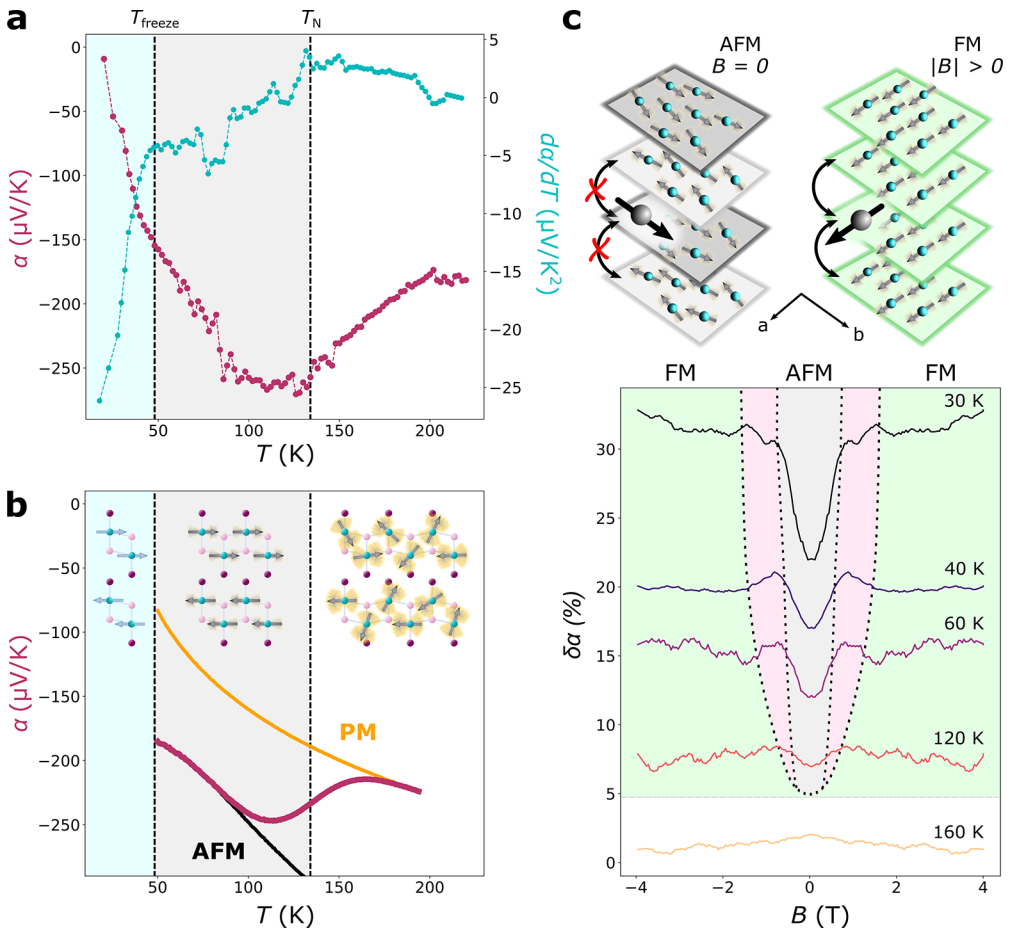

Figure 3. Magnetic field and temperature dependence of the Seebeck coefficient of CrSBr. a) Variation of the Seebeck coefficient (purple curve) and its first derivative (cyan curve) at $B = 0$ as a function of temperature. The temperatures T_N and T_{freeze} separate the graph in three areas, colored respectively in white, gray and light blue. b) First-principles Seebeck coefficient as a function of T, for a representative (n-type) doping level, calculated in the AFM (black curve), PM (orange curve), and interpolated magnetic states (purple curve). c) Magneto-Seebeck coefficient as a function of temperature. Each curve is offset by 5% for clarity, and averaged as $\frac{\delta\alpha(B)+\delta\alpha(-B)}{2}$ in order to remove any parasitic effect due to drift in the measurement. The black dotted guidelines delimit the transition region (depicted in pink) in which the spins are canting from AFM (gray area) to FM (green area) ordering and the Seebeck coefficient reaches its maximum. In particular, the external black dotted line between the transition region and the FM state represents the saturation magnetic field H_S (see Supporting Information section S9). The field-dependent spin reorientation and interlayer tunneling is illustrated in the top part of the image. The orientation of the crystallographic axes is also reported. An electron residing on one of the layers (dark gray sphere) can tunnel (indicated by the black curved arrows) or not (indicated by the black curved arrows with red X) depending on its spin orientation.

materials A-type antiferromagnet CrSBr stands out for its good cleavability as well as its Néel temperature T_N of 132 K, one of the highest reported among vdW antiferromagnets.[14,17] Compared to ferromagnets, antiferromagnetic (AFM) materials offer the possibility to change their spin structure into a field-induced ferromagnetic (FM) configuration upon the application of an external magnetic field, adding a degree of freedom in tuning the electronic and thermoelectric properties.[18,19] Each CrSBr vdW layer consists of two fused buckled planes of CrS, sandwiched between Br atoms and stacked along the c axis (see Figure 2a).[14,17] CrSBr is an A-type antiferromagnet, with intralayer FM coupling and interlayer AFM interaction, and with an easy/medium/hard axis coinciding with the crystallographic b/a/c axes, respectively.[20] Furthermore, CrSBr shows semiconducting transport properties, with a direct band gap of $E_G = 1.5$ eV and finite electrical conductivity at low temperature.[18] In particular, thanks to the strong coupling between magnetic ordering and transport properties in CrSBr, an external magnetic field can be used to alter the electrical resistance, which tends to decrease as the field increases. This comes as a consequence of the reduction of spin fluctuations, and the different interlayer spin-flip scattering between AFM and FM configurations.[17,18,20,21] While the electrical transport and magnetic properties of this material have been extensively investigated,[17,18,20−22] the effect of magnetic order on the entropy and thus the thermoelectric properties has not been reported to date.

In this paper, we study the impact of electronic and spin-entropy on the thermoelectric properties of CrSBr thin flakes. To this end, we change the magnetic order by varying the sample temperature or by applying an external magnetic field, while simultaneously measuring the electrical and thermoelectric transport properties. We observe a steep increase of the Seebeck coefficient and the thermoelectric power factor with increasing temperature as electrons and spins mobilize, with a local maximum slightly below T_N which we explain by a competition between electronic band entropy and magnetic entropy in CrSBr. We further reveal that a magnetic field can

https://doi.org/10.1021/acs.nanolett.4c00809
Nano Lett. 2024, 24, 6513−6520

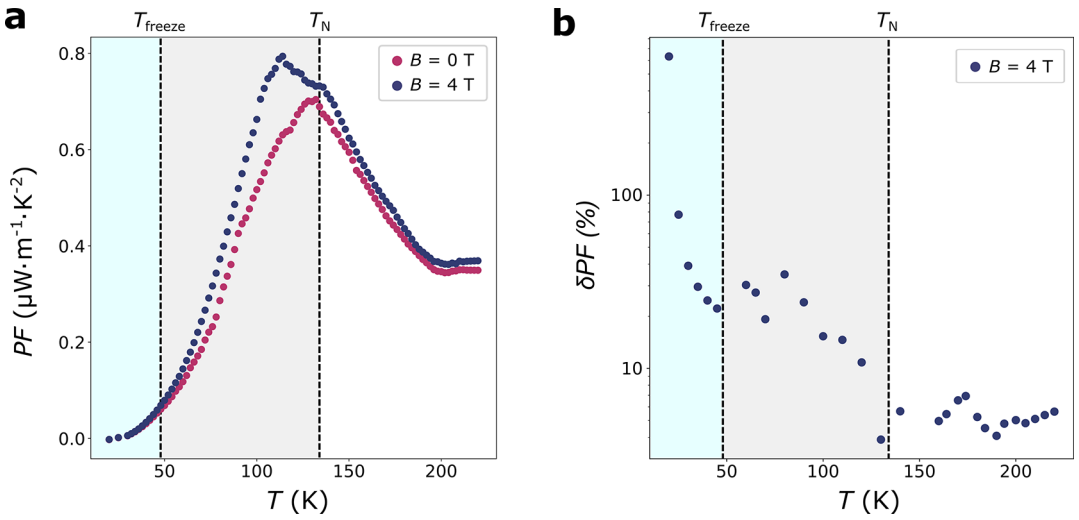

Figure 4. Field and temperature dependence of the power factor. (a) Temperature-dependent power factor, for $B = 0$ (purple) and $B = 4$ T (blue). (b) Magneto-power factor (δPF) as a function of temperature, measured at $B = 4$ T.

enhance the power factor by up to 600% at low temperatures. These findings highlight how (spin)entropy engineering in 2D magnetic materials could be used to build thermoelectric heat engines with a strongly enhanced performance.

To measure the electrical and thermoelectric properties of CrSBr thin flakes we employ a device architecture (Figure 2b–c) that we recently developed for thermoelectric experiments on single molecule junctions.[23,24] It consists of prepatterned contacts, thermometers and microheaters on top of which a CrSBr flake has been stamped using a dry transfer method.[25,26] A thin hexagonal Boron Nitride (hBN) flake is used to encapsulate CrSBr to prevent degradation and contamination (see Supporting Information sections S1–5 for details). An optical micrograph of the final device is shown in Figure 2d. For a typical measurement (Figure 2c), an AC current $\tilde{I}_h$ at frequency ω_1 is applied to the microheater which generates a temperature bias ΔT proportional to $\tilde{I}_h^2$, therefore having frequency $2\omega_1$. Simultaneously, an AC voltage $\tilde{V}_{sd}$ at frequency $\omega_2 \gg \omega_1$ is applied to the drain contact. The current to ground on the source contact is then demodulated at frequencies ω_2 and $2\omega_1$ to extract the differential conductance $G = \frac{\tilde{I}_{sd}}{\tilde{V}_{sd}}$ and the Seebeck coefficient $\alpha = -\frac{\tilde{V}_{th}}{\Delta T} = -\frac{\tilde{I}_{th}}{G\Delta T}$, by assuming $\alpha = L/G$, where L is the thermoelectric conductivity[27] (see Supporting Information section S8 for details on the temperature calibration). The frequencies ω_1 and ω_2 used in the experiments, respectively 3 and 13 Hz, are slow enough for the system to equilibrate. By using such a configuration, we are able to record simultaneously the electrical conductance and thermoelectric properties and therefore to evaluate in a more accurate way the thermoelectric properties of CrSBr, as we can exclude possible offsets/drifts that could occur when performing individual measurements. Finally, all magnetic fields in this study were applied parallel to the a (medium) axis of CrSBr.

Figure 2e illustrates the temperature dependence of G and of $\frac{d^2G}{dT^2}$, respectively. G decreases when lowering T, typical for semiconducting materials and in good agreement with previous studies.[17,18,21] Furthermore, we observe a maximum in G and a sharp dip in $\frac{d^2G}{dT^2}$ around 133 ± 1 K. We associate this value with T_N, where the transition from the PM state (white region) to the AFM one (gray region) occurs.[10,17,18,22,28] Upon further lowering T, G drops by 1 order of magnitude between T_N and 20 K.[21] At temperatures lower than $T_{freeze} = 47 \pm 2$ K, the appearance of a low-temperature magnetic hidden order has been reported.[18,22,29] We do not observe variations in G around T_{freeze}; however, as we will show later, the Seebeck coefficient changes abruptly below this temperature. G values depicted in Figure 2e are in good agreement with the conductance reported in previous works.[17,18]

In Figure 2f we show the magneto-resistance ratio $MRR = \frac{R(B) - R(B=0)}{R(B=0)} \cdot 100$ at different temperatures between 20 and 160 K. Below T_N, for low magnetic fields, spins are AFM coupled between layers and aligned along the b (easy) axis (see gray area). As reported previously, this suppresses the interlayer tunneling, and thus leads to an increase in electrical resistance.[17,18] By raising the applied magnetic field, spins tend to cant: This re-enables interlayer tunneling and therefore lowers the resistance.[17,18,30] Saturation of the MRR is visible when FM order between the layers is established (see green area).[17]

Figure 3a shows the temperature dependence of the Seebeck coefficient simultaneously measured with $G(T)$ (Figure 2e). The negative sign of α is consistent with the n-type doping typically found in CrSBr, which is attributed to Br vacancies.[17,31] We observe an overall decrease from −265 to −9 μV/K when cooling the sample from 200 to 20 K, which is the base temperature of our experiment. Three areas are highlighted by means of different colors. In the white region ($T > T_N$), corresponding to the PM phase, $|\alpha|$ increases as T decreases. $|\alpha|$ reaches its maximum at T_N, stays constant until $T \approx 90$ K, and then decreases (overall about 45%) until T_{freeze} (gray region). When cooling below T_{freeze} (light blue area), $|\alpha|$ decreases faster—as can be seen in the first derivative $d\alpha/dT$ (cyan curve)—down to the value of −9 μV/K at 20 K. To explain this behavior, we performed first-principles calculations within the constant relaxation time approximation,[32] for a doping of $\sim 8 \times 10^{18}$ electrons per cm^3 (see Supporting Information Figure S9). In Figure 3b we compare the AFM ground state, a collinear PM state (averaging special quasirandom structures[33]), and an interpolation between the

https://doi.org/10.1021/acs.nanolett.4c00809
Nano Lett. 2024, 24, 6513−6520

two.[34] The calculations are in good quantitative agreement at low and intermediate temperatures, show the same qualitative extremum and upturn around T_N, but underestimate the upward jump of α in the full PM phase. Our calculation of the bands in a collinear PM state produces a smaller Seebeck amplitude (less negative). Freeing the spins to be noncollinear PM should produce even more phase space and entropy for the spins, and therefore a larger jump. It should be noted that our first principle model is not suitable to predict $\alpha(T)$ at $T <$ 50 K. In this regime, a strong modulation of the carrier concentration is expected which is not accounted for in the calculations.

To gain further evidence for the impact of magnetic order on the thermoelectric properties of CrSBr, we measured the change in the Seebeck coefficient as a function of the applied magnetic field. Figure 3c shows this magneto-Seebeck coefficient ratio $\delta\alpha = \frac{\alpha(B) - \alpha(B=0)}{\alpha(B=0)} \cdot 100$ versus magnetic field B at temperatures varying between 20 and 160 K. At 160 K, the flake is in a PM state and the curve shows almost no variation with applied B field. Below T_N and for small magnetic fields, CrSBr is AFM ordered (gray area) and $\delta\alpha$ is minimum at B = 0. As the absolute value of B becomes larger, $\delta\alpha$ increases and reaches a local maximum, then decreases until saturating when FM order is established (green area). The areas including the local maxima of $\delta\alpha$ (in pink) can be identified as transition regions, in which the spins are canting from the a to b direction due to the application of the external B field.[22] We observe an increase in $\delta\alpha$ of up to 13% at low T when changing from AFM to FM order (see Supporting Information Figure S7 for measurements on additional CrSBr devices).

Figure 4a displays the temperature-dependent power factor $PF = \alpha^2 \cdot \sigma$, where σ is the electrical conductivity of CrSBr (see Supporting Information section S3). As part of the figure of merit zT, the power factor helps quantify the energy harvesting efficiency of the material. As it is also proportional to the maximum achievable output power, it is a useful parameter for quantifying Peltier cooling. At B = 0, PF shows a peak of 7 μW m^{-1} K^{-2} around T_N, where the maxima of G and α also simultaneously occur. This peak increases in magnitude and shifts to lower temperatures when a magnetic field of B = 4 T is applied. Figure 4b shows the magneto-power factor $\delta PF = \frac{PF(B=4\mathrm{T}) - PF(B=0)}{PF(B=0)\cdot 100}$ as a function of temperature. We observe that the relative change δPF increases with decreasing temperature and reaches values up to 600% at 20K. Below we discuss that these findings can be explained by the intrinsic band structure of AFM CrSBr, taking into account variations in the entropy linked to the magnetic order.

As we described at the beginning of this article, the Seebeck coefficient is closely linked to the entropy S of the system (see eq 1).[8,35] The entropy of a mesoscopic system can be estimated using the Boltzmann formula $S = k_B \ln(\Omega)$, where Ω represents the number of all possible microstates of the system.[1,36] Here, we assume that Ω contains three main contributions. Ω_p represents the conventional distribution of momenta of the electron gas (the electronic band contribution). Then, we take into account a layer degree of freedom Ω_{layer} which quantifies the number of layers a charge carrier can access, as CrSBr is a layered vdW material in which interlayer tunneling is precluded when switching to AFM order.[37] Lastly, we include a term Ω_s representing all possible spin configurations, which yields the spin-entropy S_m.[38] The sign of this contribution depends on the nature of the d bands hosting the magnetization, which is positive in CrSBr (hole like, from the d band valence electrons).[1] Therefore, the electronic and spin-entropy contributions have opposite signs. We now turn back to Figure 3a, which depicts the temperature dependence of α. As $T \geq T_{freeze}$, the growth of the Seebeck coefficient abruptly slows down, which is simultaneous with the appearance of a magnetic hidden order below T_{freeze}. Such hidden order was already observed previously by other groups, who associate its origin either to a magnetic coupling between self-trapped defects,[18] the anisotropic structure of CrSBr—which can be seen as weakly and incoherently coupled 1D chains[21]—or a spin-dimensionality crossover caused by a slowing down of the magnetic fluctuations (spin freezing).[22,29] The consequence of the spin freezing phenomenon is that spin fluctuations are fully suppressed (Ω_s = 1) below T_{freeze}, and therefore cannot contribute to the entropy[22] to counteract the electronic α.[1] Additionally, interlayer tunneling is suppressed (Ω_{layer} = 1).[21,22,29] As the spins mobilize upon heating, their contribution S_m is superimposed on intrinsic electronic α. Due to the opposite signs of the electronic and spin-entropy contributions, their combined action leads to a plateau and turnover when increasing T. At higher temperatures ($T \sim T_N$), two effects cause the reduction in $|\alpha|$ observed in our experiment: First, fluctuations and S_m increase as CrSBr approaches T_N, then saturate in the fully PM phase;[10,39] second, an increase in carrier concentration decreases the magnitude of α (less negative, see Supporting Information Figure S8). The subsequent increase in $|\alpha|$ beyond temperatures of 200 K, as observed in our experiments and predicted by theory, can be attributed to the dominance of Ω_p over the saturated Ω_s in the fully PM state.

Figure 3c illustrates how an external magnetic field, B, affects α. The application of B along the a direction of CrSBr produces a continuous canting of the spins.[10] Such field-induced spin reorientation initially raises Ω_s, which leads to an increase in $|\alpha|$ (pink shaded areas). When further increasing B, the FM order is established and Ω_s is minimized, reducing $|\alpha|$ again.[38,40] In addition, the transition from AFM to FM order enables interlayer tunneling and thus raises Ω_{layer} (see Figure 3c). This could explain the higher α in the FM phase compared to the AFM one and has an important consequence: Since both σ and α simultaneously increase with magnetic field, the relative change of the power factor ($\alpha^2\sigma$) between AFM and FM order can reach very high values, up to 600% as observed in our experiment (Figure 4b).

In this work, we investigate the magnetic field and temperature dependence of electric and thermoelectric properties of the A-type antiferromagnet CrSBr. We reveal a strong impact of magnetic order on the thermoelectric response of the material, which we attribute to a spin-entropy contribution to the total thermopower. In particular, we detect a peak in both the Seebeck coefficient and the power factor around the magnetic transition temperature T_N. These findings present a potential way to overcome the limits of conventional thermoelectric devices by employing magnetic materials. While devices based on CrSBr show enhanced thermoelectric properties at cryogenic temperatures, future research should investigate 2D magnets with a higher transition temperature to enable room temperature operation. Promising materials that deserve attention are the recently investigated 2D compounds $CrTe_2$ and Fe_3GaTe_2 with magnetic ordering temperatures >300 K.[41,42] To this end, the use of 2D materials adds further

https://doi.org/10.1021/acs.nanolett.4c00809
Nano Lett. 2024, 24, 6513−6520

benefits, such as the possibility to tune the transition temperature by varying the flake thickness, composition, electrostatic gating, or by producing heterostructures of different layers, in order to yield optimum performance at room temperature.[43−46]

■ ASSOCIATED CONTENT

Supporting Information

The Supporting Information is available free of charge at https://pubs.acs.org/doi/10.1021/acs.nanolett.4c00809.

Sample fabrication: Exfoliation of CrSBr flakes, Atomic Force Microscopy measurements, evaluation of the electrical conductivity σ. Device fabrication: Prepatterned thermopower contacts fabrication, CrSBr flake transfer. Thermoelectric and electrical transport measurements method and calibration. Additional field-dependent measurements of the thermoelectric properties (α, PF) of a second CrSBr flake. Evaluation of the saturation field H_S. Temperature-dependent variation of α as a function of the doping concentration. Degradation study of CrSBr flakes. First principles simulations and evaluation of the transport coefficients. (PDF)

■ AUTHOR INFORMATION

Corresponding Author

Pascal Gehring − *Institute of Condensed Matter and Nanosciences, Université Catholique de Louvain (UCLouvain), 1348 Louvain-la-Neuve, Belgium;* orcid.org/0000-0002-7073-9922; Email: pascal.gehring@uclouvain.be

Authors

Alessandra Canetta − *Institute of Condensed Matter and Nanosciences, Université Catholique de Louvain (UCLouvain), 1348 Louvain-la-Neuve, Belgium;* orcid.org/0000-0003-0119-5615

Serhii Volosheniuk − *Kavli Institute of Nanoscience, Delft University of Technology, 2628CJ Delft, The Netherlands*

Sayooj Satheesh − *Max-Planck-Institut für Festkörperforschung, D-70569 Stuttgart, Germany*

José Pedro Alvarinhas Batista − *Nanomat/Q-MAT/ and European Theoretical Spectroscopy Facility, Université de Liège, B-4000 Liège, Belgium*

Aloïs Castellano − *Nanomat/Q-MAT/ and European Theoretical Spectroscopy Facility, Université de Liège, B-4000 Liège, Belgium*

Riccardo Conte − *Kavli Institute of Nanoscience, Delft University of Technology, 2628CJ Delft, The Netherlands*

Daniel George Chica − *Department of Chemistry, Columbia University, New York, New York 10027, United States*

Kenji Watanabe − *Research Center for Electronic and Optical Materials, National Institute for Materials Science, Tsukuba 305-0044, Japan;* orcid.org/0000-0003-3701-8119

Takashi Taniguchi − *Research Center for Materials Nanoarchitectonics, National Institute for Materials Science, Tsukuba 305-0044, Japan;* orcid.org/0000-0002-1467-3105

Xavier Roy − *Department of Chemistry, Columbia University, New York, New York 10027, United States;* orcid.org/0000-0002-8850-0725

Herre S. J. van der Zant − *Kavli Institute of Nanoscience, Delft University of Technology, 2628CJ Delft, The Netherlands;* orcid.org/0000-0002-5385-0282

Marko Burghard − *Max-Planck-Institut für Festkörperforschung, D-70569 Stuttgart, Germany*

Matthieu Jean Verstraete − *Nanomat/Q-MAT/ and European Theoretical Spectroscopy Facility, Université de Liège, B-4000 Liège, Belgium; ITP, Physics Department, Utrecht University, 3508 TA Utrecht, The Netherlands*

Complete contact information is available at: https://pubs.acs.org/10.1021/acs.nanolett.4c00809

Author Contributions

P.G. conceived and supervised the experiments. S.V. fabricated the prepatterned contacts and performed the experiments, supported by R.C. and H.v.d.Z. A.C. prepared the CrSBr device, performed the experiments with the support of S.S. and M.B., and evaluated the data. A.C. and P.G. wrote the manuscript. D.C. and X.R. synthesized the CrSBr. K.W. and T.T. provided the hBN. A.Castellano, J.A.-B., and M.V. performed the first-principles simulations.

Notes

The authors declare no competing financial interest.

■ ACKNOWLEDGMENTS

P.G. acknowledges financial support from the F.R.S.-FNRS of Belgium (FNRS-CQ-1.C044.21-SMARD, FNRS-CDR-J.0068.21-SMARD, FNRS-MIS-F.4523.22-TopoBrain), and from the EU (ERC-StG-10104144-MOUNTAIN). P.G., A.C., A.Castellano, J.A-B., and M.V. acknowledge funding from the Federation Wallonie-Bruxelles through the ARC Grant No. 21/26-116, and from the FWO and FRS-FNRS under the Excellence of Science (EOS) programme (40007563-CONNECT). H.v.d.Z. acknowledges support by the FET open project QuIET (Number 767187) and by The Netherlands Organisation for Scientific Research (NWO). K.W. and T.T. acknowledge support from the JSPS KAKENHI (Grant Numbers 21H05233 and 23H02052) and World Premier International Research Center Initiative (WPI), MEXT, Japan for the growth of h-BN crystals. M.B. is grateful for support from the Deutsche Forschungsgemeinschaft (DFG) via Grant BU 1125/11-1. M.V. acknowledges a PRACE award granting access to MareNostrum4 at Barcelona Supercomputing Center (BSC), Spain and Discoverer in SofiaTech, Bulgaria (OptoSpin project id. 2020225411). Synthetic work at Columbia was supported by the National Science Foundation (NSF) through the Columbia Materials Science and Engineering Research Center on Precision-Assembled Quantum Materials (DMR-2011738).

■ REFERENCES

(1) Sun, P.; Kumar, K. R.; Lyu, M.; Wang, Z.; Xiang, J.; Zhang, W. Generic Seebeck effect from spin entropy. *Innovation* **2021**, *2*, 100101.

(2) Behnia, K. *Fundamentals of Thermoelectricity*; Oxford University Press: 2015.

(3) Apertet, Y.; Ouerdane, H.; Goupil, C.; Lecoeur, P. A note on the electrochemical nature of the thermoelectric power. *European Physical Journal Plus* **2016**, *131*, 76.

(4) Cai, J.; Mahan, G. D. Effective Seebeck coefficient for semiconductors. *Phys. Rev. B* **2006**, *74*, 075201.

(5) Chaikin, P. M.; Beni, G. Thermopower in the correlated hopping regime. *Phys. Rev. B* **1976**, *13*, 647−651.

(6) Peterson, M. R.; Shastry, B. S. Kelvin formula for thermopower. *Phys. Rev. B* **2010**, *82*, 195105.
(7) Yang, G.; Sang, L.; Zhang, C.; Ye, N.; Hamilton, A.; Fuhrer, M. S.; Wang, X. The role of spin in thermoelectricity. *Nature Reviews Physics* **2023**, *5*, 466−482.
(8) Pyurbeeva, E.; Mol, J. A.; Gehring, P. Electronic measurements of entropy in meso- and nanoscale systems. *Chemical Physics Reviews* **2022**, *3*, 041308.
(9) Shastry, B. S. In *New Materials for Thermoelectric Applications: Theory and Experiment*; Zlatic, V., Hewson, A., Eds.; Springer Netherlands: Dordrecht, 2013; pp 25−29.
(10) Tsujii, N.; Nishide, A.; Hayakawa, J.; Mori, T. Observation of enhanced thermopower due to spin fluctuation in weak itinerant ferromagnet. *Science Advances* **2019**, *5*, No. eaat5935.
(11) Wang, L.; Zhang, X.; Zhao, L.-D. Evolving Strategies Toward Seebeck Coefficient Enhancement. *Accounts of Materials Research* **2023**, *4*, 448−456.
(12) Portavoce, A.; Assaf, E.; Bertoglio, M.; Narducci, D.; Bertaina, S. Magnetic moment impact on spin-dependent Seebeck coefficient of ferromagnetic thin films. *Sci. Rep.* **2023**, *13*, 172.
(13) Yao, Y.; Zhan, X.; Sendeku, M. G.; Yu, P.; Dajan, F. T.; Zhu, C.; Li, N.; Wang, J.; Wang, F.; Wang, Z.; He, J. Recent progress on emergent two-dimensional magnets and heterostructures. *Nanotechnology* **2021**, *32*, 472001.
(14) Jiang, X.; Liu, Q.; Xing, J.; Liu, N.; Guo, Y.; Liu, Z.; Zhao, J. Recent progress on 2D magnets: Fundamental mechanism, structural design and modification. *Applied Physics Reviews* **2021**, *8*, 031305.
(15) Burch, K.; Mandrus, D.; Park, J.-G. Magnetism in two-dimensional van der Waals materials. *Nature* **2018**, *563*, 47−52.
(16) Cortie, D. L.; Causer, G. L.; Rule, K. C.; Fritzsche, H.; Kreuzpaintner, W.; Klose, F. Two-Dimensional Magnets: Forgotten History and Recent Progress towards Spintronic Applications. *Adv. Funct. Mater.* **2020**, *30*, 1901414.
(17) Telford, E. J.; Dismukes, A. H.; Lee, K.; Cheng, M.; Wieteska, A.; Bartholomew, A. K.; Chen, Y.-S.; Xu, X.; Pasupathy, A. N.; Zhu, X.; Dean, C. R.; Roy, X. Layered Antiferromagnetism Induces Large Negative Magnetoresistance in the van der Waals Semiconductor CrSBr. *Adv. Mater.* **2020**, *32*, 2003240.
(18) Telford, E.; et al. Coupling between magnetic order and charge transport in a two-dimensional magnetic semiconductor. *Nat. Mater.* **2022**, *21*, 754−760.
(19) Bauer, G. E. W.; Saitoh, E.; van Wees, B. J. Spin caloritronics. *Nat. Mater.* **2012**, *11*, 391−399.
(20) Lee, K.; Dismukes, A. H.; Telford, E. J.; Wiscons, R. A.; Wang, J.; Xu, X.; Nuckolls, C.; Dean, C. R.; Roy, X.; Zhu, X. Magnetic Order and Symmetry in the 2D Semiconductor CrSBr. *Nano Lett.* **2021**, *21*, 3511−3517. PMID: 33856213.
(21) Wu, F.; Gutiérrez-Lezama, I.; López-Paz, S. A.; Gibertini, M.; Watanabe, K.; Taniguchi, T.; von Rohr, F. O.; Ubrig, N.; Morpurgo, A. F. Quasi-1D Electronic Transport in a 2D Magnetic Semiconductor. *Adv. Mater.* **2022**, *34*, 2109759.
(22) Lopez-Paz, S. A.; Guguchia, Z.; Pomjakushin, V. Y.; Witteveen, C.; Cervellino, A.; Luetkens, H.; Casati, N.; Morpurgo, A. F.; von Rohr, F. O. Dynamic magnetic crossover at the origin of the hidden-order in van der Waals antiferromagnet CrSBr. *Nat. Commun.* **2022**, *13*, 4745.
(23) Gehring, P.; van der Star, M.; Evangeli, C.; Le Roy, J. J.; Bogani, L.; Kolosov, O. V.; van der Zant, H. S. J. Efficient heating of single-molecule junctions for thermoelectric studies at cryogenic temperatures. *Appl. Phys. Lett.* **2019**, *115*, 073103.
(24) Gehring, P.; Sowa, J. K.; Hsu, C.; de Bruijckere, J.; van der Star, M.; Le Roy, J. J.; Bogani, L.; Gauger, E. M.; van der Zant, H. S. J. Complete mapping of the thermoelectric properties of a single molecule. *Nat. Nanotechnol.* **2021**, *16*, 426.
(25) Castellanos-Gomez, A.; Buscema, M.; Zant, H.; Steele, G. Deterministic transfer of two-dimensional materials by all-dry viscoelastic stamping. *2D Materials* **2014**, *1*, 011002.
(26) Frisenda, R.; Navarro-Moratalla, E.; Gant, P.; Perez de Lara, D.; Jarillo-Herrero, P.; Gorbachev, R.; Castellanos-Gomez, A. Recent progress in the assembly of nanodevices and van der Waals heterostructures by deterministic placement of 2D materials. *Chem. Soc. Rev.* **2018**, *47*, 53−68.
(27) Lambert, C. J.; Sadeghi, H.; Al-Galiby, Q. H. Quantum-interference-enhanced thermoelectricity in single molecules and molecular films. *Comptes Rendus. Physique* **2016**, *17*, 1084−1095.
(28) Liu, W.; Guo, X.; Schwartz, J.; Xie, H.; Dhale, N. U.; Sung, S. H.; Kondusamy, A. L. N.; Wang, X.; Zhao, H.; Berman, D.; Hovden, R.; Zhao, L.; Lv, B. A Three-Stage Magnetic Phase Transition Revealed in Ultrahigh-Quality van der Waals Bulk Magnet CrSBr. *ACS Nano* **2022**, *16*, 15917−15926. PMID: 36149801.
(29) Boix-Constant, C.; Mañas-Valero, S.; Ruiz, A. M.; Rybakov, A.; Konieczny, K. A.; Pillet, S.; Baldoví, J. J.; Coronado, E. Probing the Spin Dimensionality in Single-Layer CrSBr Van Der Waals Heterostructures by Magneto-Transport Measurements. *Adv. Mater.* **2022**, *34*, 2204940.
(30) Ye, C.; Wang, C.; Wu, Q.; Liu, S.; Zhou, J.; Wang, G.; Söll, A.; Sofer, Z.; Yue, M.; Liu, X.; Tian, M.; Xiong, Q.; Ji, W.; Renshaw Wang, X. Layer-Dependent Interlayer Antiferromagnetic Spin Reorientation in Air-Stable Semiconductor CrSBr. *ACS Nano* **2022**, *16*, 11876−11883. PMID: 35588189.
(31) Klein, J.; et al. The Bulk van der Waals Layered Magnet CrSBr is a Quasi-1D Material. *ACS Nano* **2023**, *17*, 5316−5328. PMID: 36926838.
(32) Madsen, G. K.; Carrete, J.; Verstraete, M. BoltzTraP2, a program for interpolating band structures and calculating semi-classical transport coefficients. *Comput. Phys. Commun.* **2018**, *231*, 140−145.
(33) Zunger, A.; Wei, S.-H.; Ferreira, L. G.; Bernard, J. E. Special quasirandom structures. *Phys. Rev. Lett.* **1990**, *65*, 353−356.
(34) Körmann, F.; Grabowski, B.; Dutta, B.; Hickel, T.; Mauger, L.; Fultz, B.; Neugebauer, J. Temperature Dependent Magnon-Phonon Coupling in bcc Fe from Theory and Experiment. *Phys. Rev. Lett.* **2014**, *113*, 165503.
(35) Sun, Z.; Wang, H.; Wang, A.; Lei, B.; Zhuo, W.; Yu, F.; Zhou, X.; Ying, J.; Xiang, Z.; Wu, T.; Chen, X. Large Thermopower Enhanced by Spin Entropy in Antiferromagnet $EuMnSb_2$. *Adv. Funct. Mater.* **2022**, *32*, 2202188.
(36) Demirel, Y.; Gerbaud, V. In *Nonequilibrium Thermodynamics*, 4th ed.; Demirel, Y., Gerbaud, V., Eds.; Elsevier: 2019; pp 603−662.
(37) Wilson, N.; Lee, K.; Cenker, J.; Xie, K.; Dismukes, A.; Telford, E.; Fonseca, J.; Sivakumar, S.; Dean, C.; Cao, T.; Roy, X.; Xu, X.; Zhu, X. Interlayer electronic coupling on demand in a 2D magnetic semiconductor. *Nat. Mater.* **2021**, *20*, 1657.
(38) Wang, Y.; Rogado, N. S.; Cava, R. J.; Ong, N. P. Spin entropy as the likely source of enhanced thermopower in $Na_xCo_2O_4$. *Nature* **2003**, *423*, 425−428.
(39) Okabe, T. Spin-fluctuation drag thermopower of nearly ferromagnetic metals. *J. Phys.: Condens. Matter* **2010**, *22*, 115604.
(40) Bonner, J. C.; Fisher, M. E. The Entropy of an Antiferromagnet in a Magnetic Field. *Proceedings of the Physical Society* **1962**, *80*, 508.
(41) Wu, H.; Zhang, W.; Yang, L.; Wang, J.; Li, J.; Li, L.; Gao, Y.; Zhang, L.; Du, J.; Shu, H.; Chang, H. Strong intrinsic room-temperature ferromagnetism in freestanding non-van der Waals ultrathin 2D crystals. *Nat. Commun.* **2021**, *12*, 5688.
(42) Zhang, X.; et al. Room-temperature intrinsic ferromagnetism in epitaxial $CrTe_2$ ultrathin films. *Nat. Commun.* **2021**, *12*, 2492.
(43) Li, D.; Gong, Y.; Chen, Y.-X.; Lin, J.; Khan, Q.; Zhang, Y.; Li, Y.; Xie, H. Recent Progress of Two-Dimensional Thermoelectric Materials. *Nano-Micro Letters* **2020**, *12*, 36.
(44) Razeghi, M.; Spiece, J.; Oğuz, O.; Pehlivanoğlu, D.; Huang, Y.; Sheraz, A.; Başçı, U.; Dobson, P.; Weaver, J.; Gehring, P.; Kasirga, S. Single-material MoS_2 thermoelectric junction enabled by substrate engineering. *npj 2D Materials and Applications* **2023**, *7*, 36.
(45) Tu, S.; et al. Record thermopower found in an IrMn-based spintronic stack. *Nat. Commun.* **2020**, *11*, 2023.
(46) Oh, J.; Kim, Y.; Chung, S.; Kim, H.; Son, J. G. Fabrication of a MoS_2/Graphene Nanoribbon Heterojunction Network for Improved

https://doi.org/10.1021/acs.nanolett.4c00809
Nano Lett. 2024, 24, 6513−6520

Thermoelectric Properties. *Advanced Materials Interfaces* **2019**, *6*, 1901333.

https://doi.org/10.1021/acs.nanolett.4c00809
Nano Lett. 2024, 24, 6513−6520